

PL-TR-96-2148

MODELING AND POST MISSION DATA ANALYSIS

V. A. Davis

**Maxwell Laboratories, Inc.
S-Cubed Division
P. O. Box 1620
La Jolla, California 92038-1620**

20 June 1996

**Final Report
May 17, 1993 to May 16, 1996**

Approved for Public Release; Distribution Unlimited.



**PHILLIPS LABORATORY
Directorate of Geophysics
AIR FORCE MATERIEL COMMAND
HANSCOM AFB, MA 01731-3010**

19961212 075

DMIC QUALITY INSPECTED 1

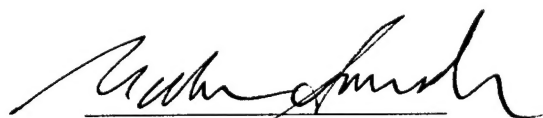
This technical report has been reviewed and is approved for publication.



DAVID G. OLSON, Capt, USAF
Contract Manager
Space Plasmas and Fields Branch
Space Physics Division



DAVID A. HARDY, Chief
Space Plasmas and Fields Branch
Space Physics Division



WILLIAM SWIDER
Deputy Director
Space Physics Division

This report has been reviewed by the ESC Public Affairs Office (PA) and is releasable to the National Technical Information Service (NTIS).

Qualified requestors may obtain additional copies from the Defense Technical Information Center. All others should apply to the National Technical Information Service.

If your address has changed, or if you wish to be removed from the mailing list, or if the addressee is no longer employed by your organization, please notify PL/TSI, Hanscom AFB, MA 01731-3010. This will assist us in maintaining a current mailing list.

Do not return copies of this report unless contractual obligations or notices on a specific document require that it be returned.

REPORT DOCUMENTATION PAGE			Form Approved OMB No. 0704-0188
<p>Public reporting burden for this collection of information is estimated to average 1 hour per response, including the time for reviewing instructions, searching existing data sources, gathering and maintaining the data needed, and completing and reviewing the collection of information. Send comments regarding this burden estimate or any other aspect of this collection of information, including suggestions for reducing this burden, to Washington Headquarters Services, Directorate for Information Operations and Reports, 1215 Jefferson Davis Highway, Suite 1204, Arlington VA 22202-4302, and to the Office of Management and Budget, Paperwork Reduction Project (0704-0188), Washington, DC 20503.</p>			
1. AGENCY USE ONLY (Leave blank)	2. REPORT DATE 20 June 1996	3. REPORT TYPE AND DATES COVERED Final Report (May 17, 1993 - May 16, 1996)	
4. TITLE AND SUBTITLE Modeling and Post Mission Data Analysis		5. FUNDING NUMBERS PE 63410F PR 2822 TA GO WU SC Contract F19628-93-C-0050	
6. AUTHOR(S) V. A. Davis			
7. PERFORMING ORGANIZATION NAME(S) AND ADDRESS(ES) Maxwell Laboratories, Inc. S-Cubed Division P O Box 1620 La Jolla CA 92038-1620		8. PERFORMING ORGANIZATION REPORT NUMBER SSS-DPR-95-15456	
9. SPONSORING/MONITORING AGENCY NAME(S) AND ADDRESS(ES) Phillips Laboratory 29 Randolph Road Hanscom AFB, MA 01731-3010		10. SPONSORING/MONITORING PL-TR-96-2148	
11. SUPPLEMENTARY NOTES			
12a. DISTRIBUTION/AVAILABILITY STATEMENT Approved for public release; distribution unlimited		12b. DISTRIBUTION CODE	
13. ABSTRACT (Maximum 200 words) This report describes work performed to do analysis in support of three Phillips laboratory flight experiments. The PASP Plus effort is an examination of the interactions of the PASP Plus spacecraft and test solar cells with the low-energy plasma environment. The SPREE effort is the use of comparison with flight data to examine, improve, and validate sheath and electron collection models and to examine some of the interactions that determine the spectrum of the incident ions. The CHAWS effort is the development and validation of models of the spacecraft wake, including the currents to the various detectors of the CHAWS wake-side sensor on the Wake Shield Facility.			
14. SUBJECT TERMS Photovoltaic Array Power Plus Diagnostics (PASP Plus), Shuttle Potential and Return Electron Experiment (SPREE), Charging Hazards and Wake Studies (CHAWS), solar array parasitic current collection, Tethered Satellite System (TSS-1), electrodynamic tether, spacecraft charging, Wake Shield Facility (WSF), spacecraft wakes		15. NUMBER OF PAGES 36	
		16. PRICE CODE	
17. SECURITY CLASSIFICATION OF REPORT Unclassified	18. SECURITY CLASSIFICATION OF THIS PAGE Unclassified	19. SECURITY CLASSIFICATION OF ABSTRACT Unclassified	20. LIMITATION OF ABSTRACT SAR

TABLE OF CONTENTS

<u>Section</u>		<u>Page</u>
1.	INTRODUCTION	1
1.1	PASP PLUS.....	1
1.2	SPREE.....	3
1.3	CHAWS.....	4
2.	DOCUMENTATION FOR SOLAR PROGRAM	7
2.1	Cell Properties.....	7
2.2	Array Properties.....	8
2.3	Environment Parameters.....	9
2.4	Current Collected.....	10
2.5	Single Cell Electron Current Collection.....	10
2.6	Single Cell Ion Current Collection.....	11
2.7	Solar Cell Sheath Width Model.....	11
2.8	Solar Array Current.....	12
2.9	Keyword Input.....	12
3.	MEASUREMENT OF NEGATIVE CHARGING ION DISTRIBUTION DURING TSS-1	14
3.1	Anisotropic Ion Flux.....	14
3.2	SPREE Measurements During DEP1 Operations.....	21
3.3	Shunter Orbit.....	23
3.4	Conclusions.....	26
4.	EPSAT WAKE STUDIES SCREEN	27
4.1	Densities.....	27
4.2	Solution Technique for Normal Orientation and Point Directly Behind Disk	28
4.3	Solution Technique for Normal Orientation and Point Not Directly Behind Disk	29
4.4	Solution Technique for Other Orientations	30
4.5	Current Densities	32

1. INTRODUCTION

This contract involves research in support of three Phillips Laboratory flight experiments, PASP Plus, SPREE, and CHAWS.

1.1 PASP PLUS

The objective of the PASP Plus analysis portion of this contract is to examine the interactions of the PASP Plus spacecraft and test solar cells with the low-energy plasma environment. Using calculational and experimental data, we developed validated models of the parasitic current collection by the test arrays.

The primary contributors to this portion of the contract were Dr. Victoria A. Davis and Ms. Barbara Gardner.

During the first year, we gathered information on the PASP Plus arrays including a site visit to Orbital Sciences Corporation.

We identified the major physical interactions that control the collection of parasitic current from the space plasma environment during flight. The equilibrium potential of the insulating surfaces exposed to the plasma depends on geometric shielding from the plasma, barrier shielding from the plasma, and the orientation of the surface with respect to the ram. Barrier formation may play a role at the lower biases, particularly for module 3. Barrier formation occurs at higher biases under laboratory conditions than under space conditions. Snapover plays a major role in determining the current collected.

We examined the PASP Plus floating potential. In order to determine the floating potential, we need to characterize the electron collection of the biased test solar array, the electron collection of the power solar array, and the ion collection of the spacecraft body. The ion collection of the spacecraft body was characterized using the NASCAP/LEO computer code. Chapter 2 of PL-TR-94-2212, ADA295230, Scientific Report No. 1, describes this work.

We modified the EPSAT electron density model so that it can model the 1000 km to 2000 km regime that IRI-86 does not properly model. Chapter 3 of PL-TR-94-2212, ADA295230, Scientific Report No. 1 describes this extension.

During the first and second years, using the Gilbert code, we examined in detail the current collection properties of a single interconnect or solar cell gap. We developed a formula for all of the solar array geometries that were flown that gives the current collected as a function of the plasma and electrical parameters. The calculational technique has been automated. We adjusted our computational algorithms to include some additional effects that examination of the experimental results suggest are important. A discussion of this work is in Chapter 2 of PL-TR-95-2095, ADA301487, Scientific Report No. 2.

We modeled the experiment panels of PASP Plus to look for any interference of sheaths and the range of plasma and electrical parameters at which interference might affect the experiment results. A discussion of this work is in Chapter 3 of PL-TR-95-2095, ADA301487, Scientific Report No. 2.

We modified the solar array module of the EPSAT computer code for use by this project. The current to a solar array is now computed by adding together the current to all the interconnects, gaps, and edges of the solar cells. Information on the environment is used by the formula the computes the current to each interconnect, gap, or edge. Updated documentation is included in Chapter 12 of PL-TR-95-2095, ADA301487, Scientific Report No. 2.

During the second and third years, we examined flight data. We confined ourselves primarily to data collected with the emitter off (so that density measurements are available) and with the solar arrays facing the ram. We compared the Langmuir probe measurements with models. We examined current collection as a function of bias and plasma density, variation within a measurement, and APEX current collection characteristics and floating potential. We compared the measurements with calculations, explored some possible reasons for the scatter in the data, and examined current collection under negative bias, and collection by the APSA array. These investigations are discussed in Chapters 4 through 11 of PL-TR-95-2095, ADA301487, Scientific Report 2 for this contract.

We wrote a stand alone computer program that implements the parasitic current collection model implemented in EPSAT. Documentation is in Chapter 2.

We presented a paper "Parasitic Current Collection in LEO" at the SPRAT conference at NASA/LeRC in Cleveland OH. (Davis and Gardner, *Proceedings of the XII Space Photovoltaic Research and Technology Conference*, NASA CP 3278, p. 227)

We presented a paper "Parasitic Current Collection by Solar Arrays in LEO" at the Aerospace Sciences Meeting and Exhibit in Reno, NV. (Davis and Gardner, AIAA 95-0594)

We prepared a paper on Modeling of Parasitic Current Collection by Solar Arrays in Low Earth Orbit. It will be completed and submitted under a related PL contract.

1.2 SPREE

The objective of the SPREE analysis portion of this contract is to use comparisons with flight data to examine, improve, and validate sheath and electron collection models and to examine some of the interactions that determine the spectrum of the incident ions.

The primary contributors to this portion of the contract were Dr. Gary A. Jongeward, Dr. Ira Katz, and Dr. Victoria A. Davis.

During the first year, we developed a module for EPSAT that examines effluent ionization for shuttle thrusters. We defined 860 lb thrusters and computed the ionization due to the interaction of the electron beam and the thruster effluent. We added a module that computes the density of ions created by effluent ionization as a function of position. We developed a detector module that computes the flux of ions created by effluent ionization to the detector. Chapter 4 of PL-TR-94-2212, ADA295230, Scientific Report No. 1 describes this work.

During the second year, we used the EPSAT model to compare the computed spectrum with SPREE measurements for a period during which the FPEG beam was perpendicular to the Earth's magnetic field. This is the event described in Hardy, *et al.*

(Observations of Electron Beam Propagation Perpendicular to the Earth's Magnetic Field during the TSS 1 Mission). A discussion of the calculation is in Chapter 13 of PL-TR-95-2095, Scientific Report No. 2 and documentation for the model is in Chapter 14 of PL-TR-95-2095, ADA301487, Scientific Report No. 2.

During the third year, we worked on a comparison of the shuttle floating potential as measured by SPREE with the Floating potential determined from the magnetic field, velocity, and tether current. This work is described in Chapter 3.

We estimated the LC time constant for the shuttle charging process to be 15 Hz. This does not provide a physical explanation for the 1 Hz modulation of the ram flux seen in daylight by SPREE under some conditions.

We assisted Phillips Laboratory staff with a paper on thruster induced charging.

The paper "Observations of Ionosphere Heating in the TSS-1 Subsatellite Presheath" was published in the May 1, 1994 issue of *Journal of Geophysical Research*. (Katz, *et al*, JGR, 99, p. 8961).

We presented a paper "Observations of Ionosphere Heating in the TSS-1 Subsatellite Presheath" at the 4th International Conference on Tethers in Space in Washington, DC.

1.3 CHAWS

The objective of the CHAWS analysis portion of this contract is to develop and validate models of the spacecraft wake, including the currents to the various detectors of the CHAWS wake side sensor on the Wake Shield Facility.

The primary contributors to this portion of the contract were Dr. Victoria A. Davis and Dr. Myron M. Mandell.

During the first year, we used our two-dimensional computational tools to compute the current to a probe behind a disk in the geometry used in the Hanscom laboratory tank. Chapter 5 of PL-TR-94-2212, ADA295230, Scientific Report No. 1 describes this work.

We used our two-dimensional computational tools to estimate the relative importance of the thermal and electrostatic effects for the flight experiment. Chapter 6 of PL-TR-94-2212, ADA295230, Scientific Report No. 1 describes this work.

We used DynaPAC to compute the current collected by the CHAWS wake side detectors for a range of flight conditions. We developed a scheme for interpolating to additional conditions. We examined the effect on current collection of the high voltage screen and grounded current collection plate design. Chapter 7 of PL-TR-94-2212, ADA295230, Scientific Report No. 1 describes this work.

We developed a screen dipole model that reproduces some of the qualitative features of the three-dimensional calculations. Chapter 8 of PL-TR-94-2212, ADA295230, Scientific Report No. 1 describes this model.

We developed two new modules for the EPSAT computer code. The Wake Studies module explores the density and current to a detector in the ambient plasma or behind a disk in the neutral approximation. This module was revised through the contract. The final documentation is in Chapter 4. The new CHAWS Current Module gives the current to the wake side probe as computed by the DynaPAC and POLAR computer codes. Chapter 10 of PL-TR-94-2212, Scientific Report No. 1 describes this module.

The geomagnetic coordinates were added to the Magnetic Field at a Point screen of EPSAT. Chapter 11 of PL-TR-94-2212, ADA295230, Scientific Report No. 1 describes the implementation.

The EPSAT floating potential model was modified to include the effect of the variation in the $v \times B$ potential across an object. Chapter 12 of PL-TR-94-2212, ADA295230, Scientific Report No. 1 describes this implementation. Two new subscreens to the floating potential screen were added. One shows the minimum and maximum potentials at the corners of each object. The other allows the user to display the "surface" potential on the entire system.

We used the measurements of the secondary emission yield of stainless steel made at Hanscom as a basis for a formula for the secondary emission as a function of incident

particle energy and species. Chapter 13 of PL-TR-94-2212, ADA295230, Scientific Report No. 1 describes this work.

During the second year, we examined data collected during the flight. We wrote some simple computer programs to assist us in the data analysis.

The EPSAT model of WSF and the shuttle was modified to obtain better values of the floating potential. Hidden surfaces of the engine bells that cannot collect current were defined to be insulating so that they do not collect ram current. The WSF carrier was added to the EPSAT model.

We did rough calculations of the fraction of phase space of the ram ions incident on WSF that reach the center of the wake side of the disk.

We presented a paper "CHAWS Wake Side Current Measurements: Comparison with Preflight Predictions" at the 33rd Aerospace Sciences Meeting in Reno, NV. (Mandell, *et al*, AIAA 95-0489).

2. DOCUMENTATION FOR SOLAR PROGRAM

Parasitic current collection is determined by the solar array, the plasma environment, and the applied bias. The user can input values that describe the array and the plasma environment. The program solar generates an iv-curve.

2.1 Cell Properties

$\Delta\phi$ = Potential generated by a single solar cell.

V_{snap} = Snapover Potential (First Crossover Energy)

m_i = Ion Current Slope

T_{cell} = Cell Thickness

D_{gap} = Gap Width

T_{cg} = Coverglass and Adhesive Thickness

T_{adh} = Adhesive Thickness

T_o = Coverglass Overhang

Figure 1 illustrates the solar cell gap region which is modeled using the above parameters.

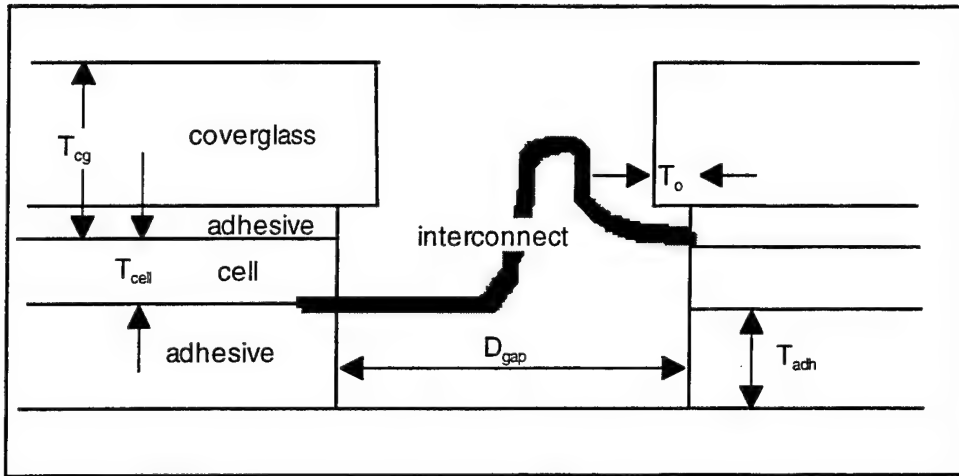


Figure 1. Solar cell gap region.

2.2 Array Properties

L_i = Total Interior Length without Interconnect

L_{ic} = Total Interconnect Length

L_e = Total Edge Length without Metal

L_m = Total Edge Length with Metal

N = Number of Cells per Series

N_s = Number of Series

The array geometry is shown in Figure 2.

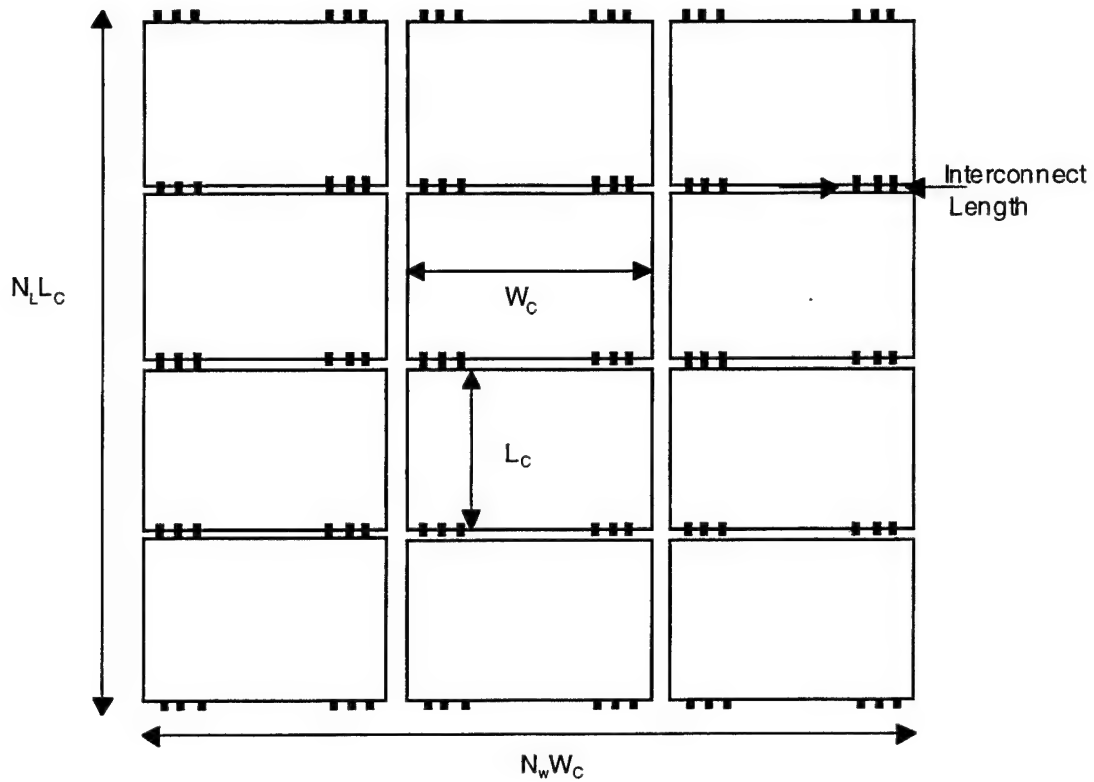


Figure 2. Solar Array with 12 cells in series.

The relationship between the cell properties and the array properties for this array is:

$$L_{ic} = \text{Interconnect length} * \text{number between cells}$$

$$L_m = \text{Interconnect length} * \text{number along edges}$$

$$L_e = 2N_w W_c + 2N_l L_c - L_m$$

$$L_i = (N_w - 1)N_l L_c + (N_l - 1)N_w W_c - L_{ic}$$

2.3 Environment Parameters

n_0 = Plasma Density

θ = Plasma Temperature

2.4 Current Collected

The current collected from the plasma by a solar cell is collected on the sides of the solar cell, and by the interconnects, if any. It is calculated as the product of the solar cell effective collecting area and the incident current density of the attracted species. The attracted species depends on whether the cell potential with respect to the plasma is positive or negative.

The effective area is a function of the electrical and geometric properties of the cell and environmental parameters and is calculated as described below.

2.5 Single Cell Electron Current Collection

For electrons the effective collecting area is calculated as the sum of four terms:

$$A_{\text{coll}}(\phi_c) = \frac{L_{ic} W_s^{ic}(\phi_c) + L_i W_s^i(\phi_c) + L_e W_s^e(\phi_c) + L_m W_s^{ic}(\phi_c)}{N} \quad (1)$$

Where,

A_{coll} = Solar cell effective collecting area

W_s^{ic} = Sheath width for interconnects

W_s^i = Sheath width for gaps without an interconnect

W_s^e = Sheath width for edges

ϕ_c = Solar cell potential with respect to the plasma

The area is computed from several two-dimensional segments. It is the distance along the solar cell edge times the length of the two-dimensional sheath. The technique to calculate the sheath width is described in the section "Solar Cell Sheath Width Model."

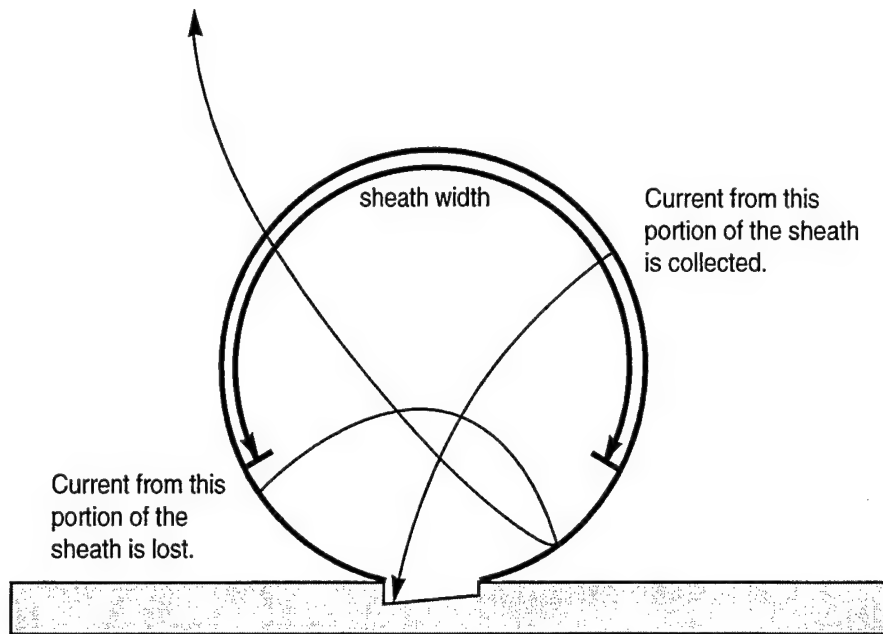


Figure 3. Solar cell gap with sheath.

2.6 Single Cell Ion Current Collection

Ion collection, which occurs when the cell potential is negative with respect to the plasma, is given as a linear function of the cell potential. The effective collecting area is as follows:

$$A_{\text{coll}}(\phi_C) = m_i \phi_C \quad (2)$$

2.7 Solar Cell Sheath Width Model

The two-dimensional electron collecting sheath width for a solar cell is modeled using the following formula:

$$S.W. = 1.1 A_{\text{geom.}} B(\eta) \frac{\phi^{0.35}}{\max(0.1, \eta)^{0.65}} \exp \left(\frac{0.63}{\lambda^{0.7}} + \frac{1}{\max(0.1, \eta)} \left(0.44 - \frac{7}{\phi} - \frac{1.13}{\lambda^{0.7}} \right) \right) \quad (3)$$

where the function B is

$$B(\eta) = \begin{cases} 1/3 & \text{no interconnect geometry and } \eta > 0.6 \\ 1 & \text{otherwise} \end{cases}$$

$$\eta = \min(1, \text{1st crossover potential}/\text{cell potential}) = \min(1, V_{\text{snap}}/\phi_c)$$

$$\phi = \text{Cell potential}/\text{plasma temperature} = \phi_c/\theta$$

$$\lambda = \text{Debye length}/\text{cell thickness} = \sqrt{\epsilon_0 \theta / e n_o} / T_{\text{cell}}$$

This formula should not be applied to scaled potential values greater than 500/0.05.

2.8 Solar Array Current

The solar array is assumed to be negatively grounded.

To get the total current collected by the solar array, we sum the currents to all the solar cells as follows:

$$I_{\text{sa}}(\phi_a) = N_s \sum_{n=1}^N A_{\text{coll}}(\phi_a + n\Delta\phi) j_{\text{th}}^a(\phi_a + n\Delta\phi) \quad (4)$$

Where,

$$j_{\text{th}}^a(\phi) = \begin{cases} j_{\text{th}}^e = e n_o \sqrt{\frac{e \theta}{2\pi m_e}} & \text{if } \phi \geq 0 \\ j^i & \text{if } \phi < 0 \end{cases} = \text{attracted current} \quad (5)$$

ϕ_a = Array Potential

2.9 Keyword Input

This program uses keyword input. The input stream consists of a list of keywords and values as given in Table 1. The END keyword signals that a current-voltage curve is to be generated with the present values. Any number (up to 1000) of sets of input parameters separated by the END keyword may be included. Execution stops when an end-of-file is sensed.

Table 1. Keywords for Input

Keyword	Symbol Used	Units	Description
	Above		
BIAS	V_1, V_2, N_{pot}	V	First potential, last potential, and number of potentials on IV curve
POTENTIAL	$\Delta\phi$	V	Potential generated by a single solar cell.
SNAP	V_{snap}	V	Snapover Potential (First Crossover Energy)
ISLP	m_i	$m^2 V^{-1}$	Ion Current Slope
CELL	T_{cell}	m	Cell Thickness
GAP	D_{gap}	m	Gap Width
CVGL	T_{cg}	m	Coverglass and Adhesive Thickness
GLUE	T_{adh}	m	Adhesive Thickness
OVHG	T_o	m	Coverglass Overhang
LNI	L_i	m	Total Interior Length without Interconnect
LI	L_{ic}	m	Total Interconnect Length
LE	L_e	m	Total Edge Length without Metal
LEM	L_m	m	Total Edge Length with Metal
NUMBER	N		Number of Cells per Series
DENSITY	n_o	m^{-3}	Plasma Density
TEMP	θ	eV	Plasma Temperature
IONS	j^i	$A m^{-2}$	Incident Ion Current Density
END			End of Data Set

3. MEASUREMENT OF NEGATIVE CHARGING ION DISTRIBUTIONS DURING TSS-1

Identification of peaks in ion and electron energy spectra have been used for decades by researchers to determine charging levels on spacecraft. During the TSS-1 mission, a computer performed this analysis in real time and provided orbiter potentials to the crew and ground controllers. TSS-1 was a unique opportunity to test the automated charging level analysis, because, for the voltages achieved during the first mission, the tethered subsatellite acted as a floating probe, and provided an independent measure of the charging potential. Below we present examples of the highly anisotropic ion spectral data collected during the mission, potentials calculated in real time using this data, and show comparisons with potentials derived using tether current and voltage measurements.

3.1 Anisotropic Ion Flux

Figure 4a shows the ion flux to SPREE as a function of bin as the instrument rotates for day 218 at 2:36:02 GMT. Figure 4b shows the same ion flux as a function of incident energy. At the time the potential decays, (as the FPEG is turned off), the aperture is facing the ram direction. Note that the bin (angle) which receives the peak current moves from 5 to 0 as the particle energy shifts from 40 to 0 V. The anisotropic, beaming of ions seen here is consistent with a local potential structure around the instrument, that is strong electric fields near the instrument, and not a uniformly charged orbiter.

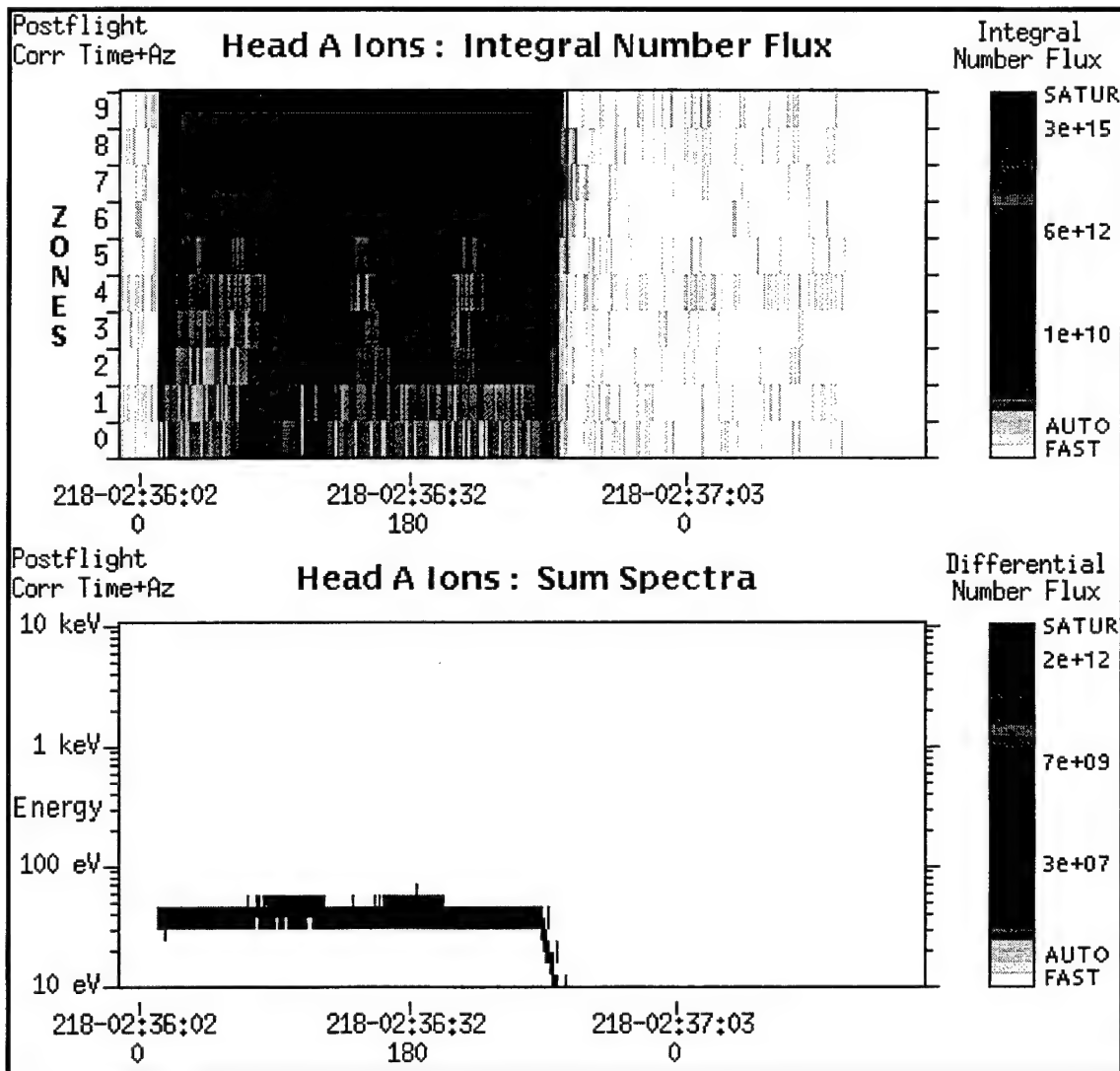


Figure 4. Ion flux to SPREE as the instrument rotates for day 218 at 2:36:02 GMT.
 (a) shows the ion flux as a function of bin. (b) shows the ion flux as a function of incident energy.

We did a series of calculations to determine the local potential structure and typical particle trajectories. Figure 5 shows a model of the SPREE instrument and the near by Langmuir probe. This model is placed in the nested grid structure shown in Figure 6. The coordinate system is +X toward the nose, +Y toward the starboard wing, and +Z into the bay. The space potentials and sheath currents

were computed for this model in a $5 \times 10^{10} \text{ m}^{-3}$, 0.1 eV plasma with a velocity of 7700 m s^{-1} in the minus X direction. This plasma density is consistent with the measured tether current of 1.7 mA and an ion collecting area on the engine bells of about 25 square meters.

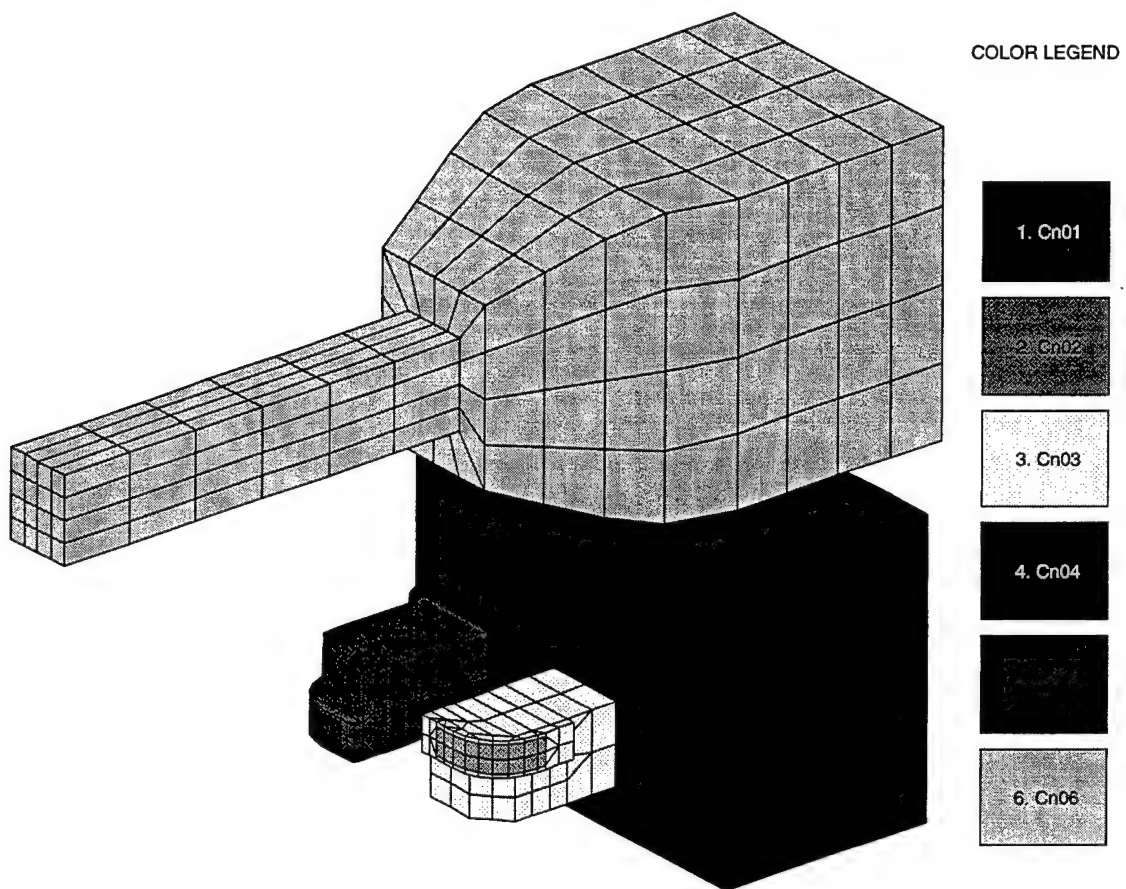


Figure 5. Model of SPREE instrument and Langmuir probe.

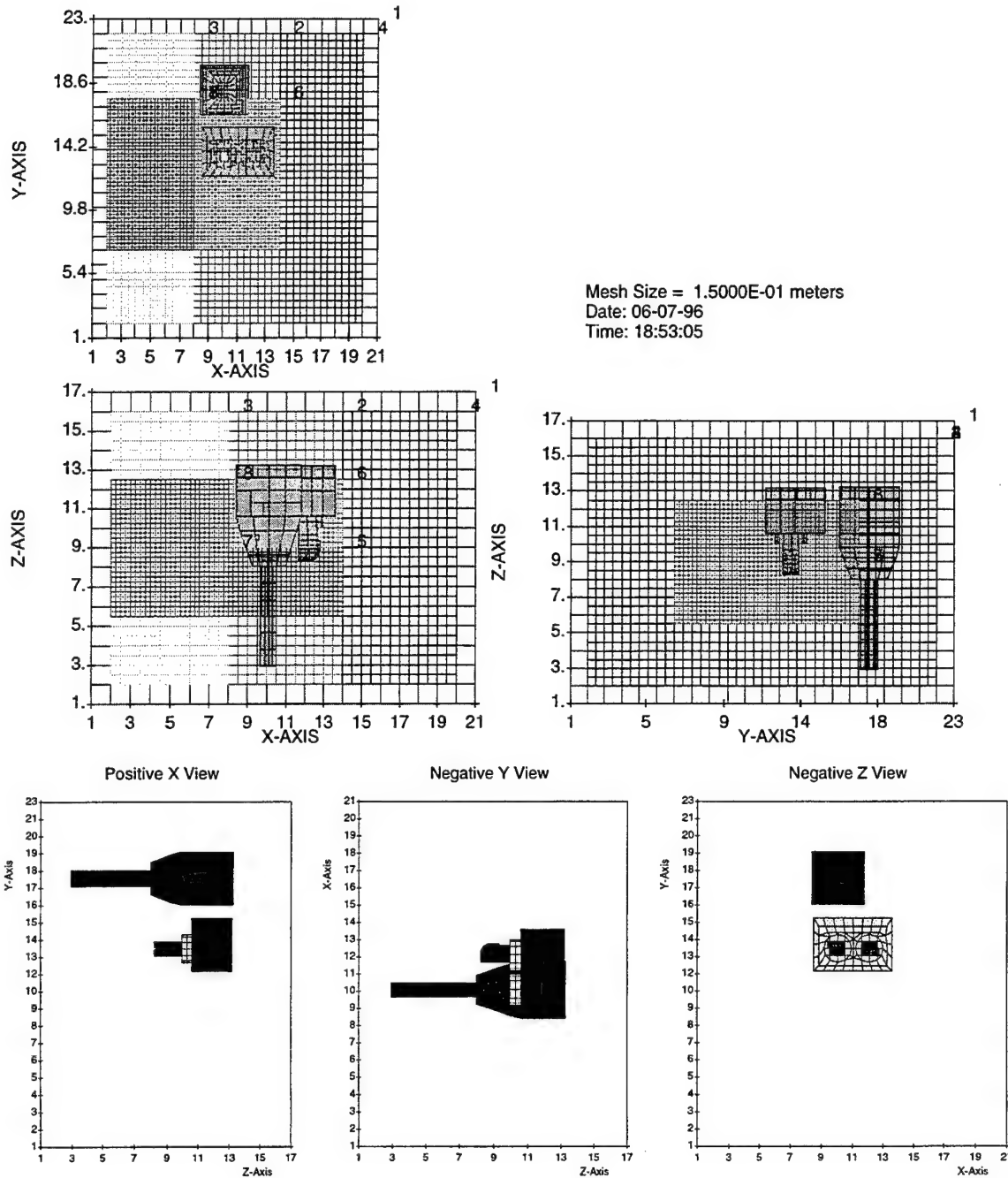


Figure 6. Grid Structure used for calculations.

Figure 7 shows the computed potentials for 37.5 V. Figure 8 shows some typical trajectories in the potentials shown in Figure 7.

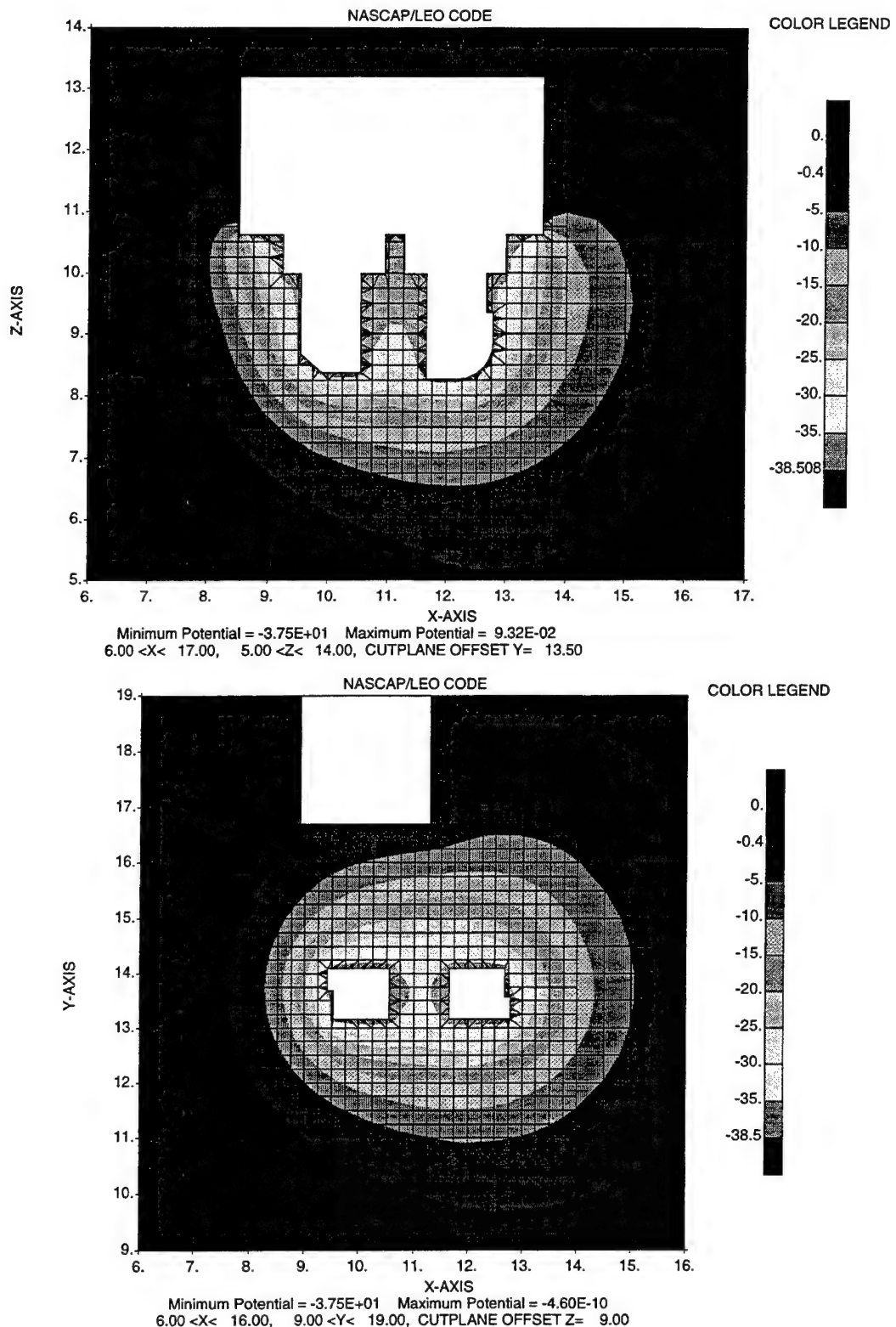


Figure 7. Computed Potentials for a ground potential of 37.5. V.

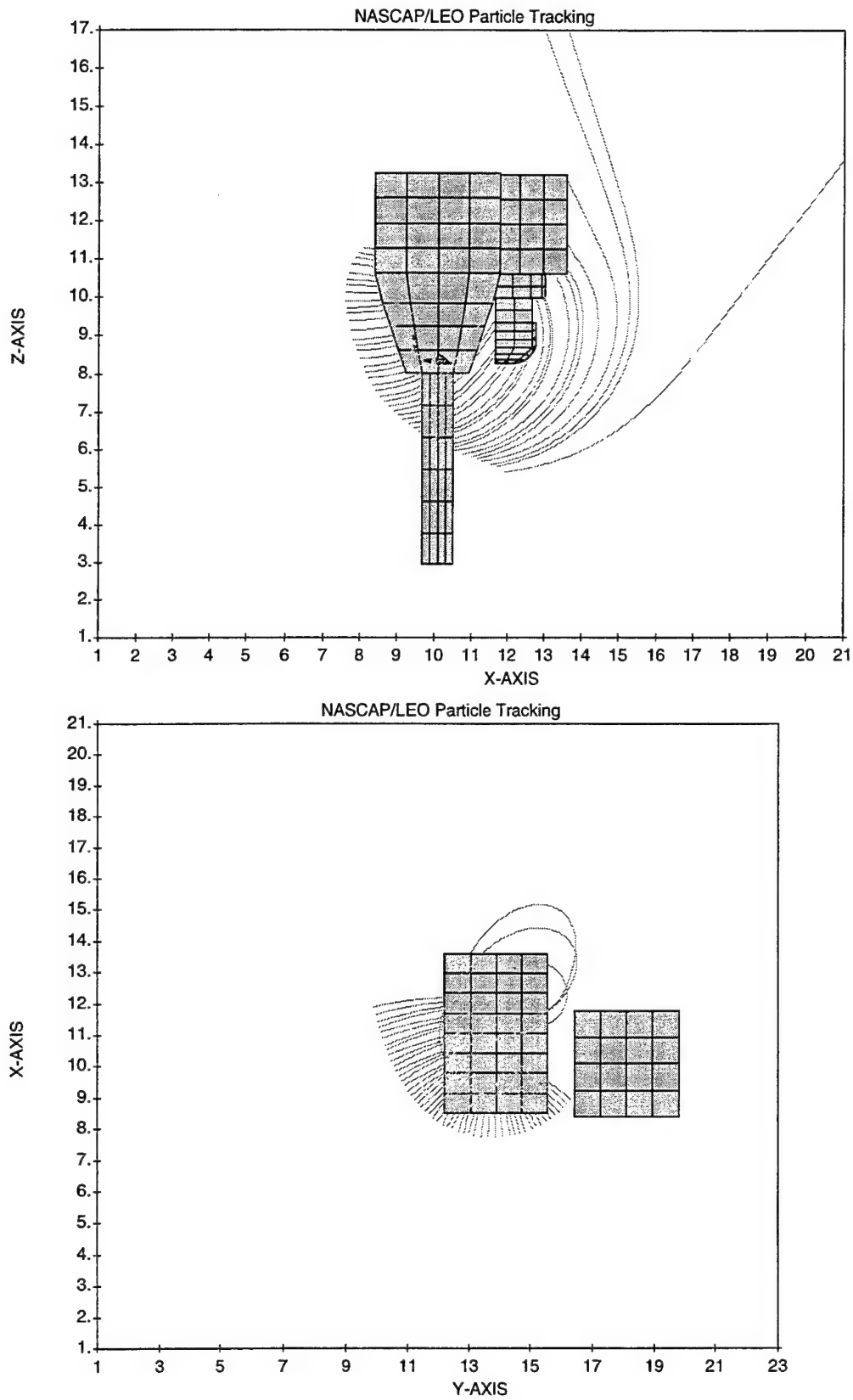


Figure 8. Typical Trajectories for potentials shown in Figure 7.

From the total collected current we sorted out the current that would be measured by SPREE. We used Figure 9 to determine the aperture location in grid coordinates to be (10.3, 13.95, 8.9).

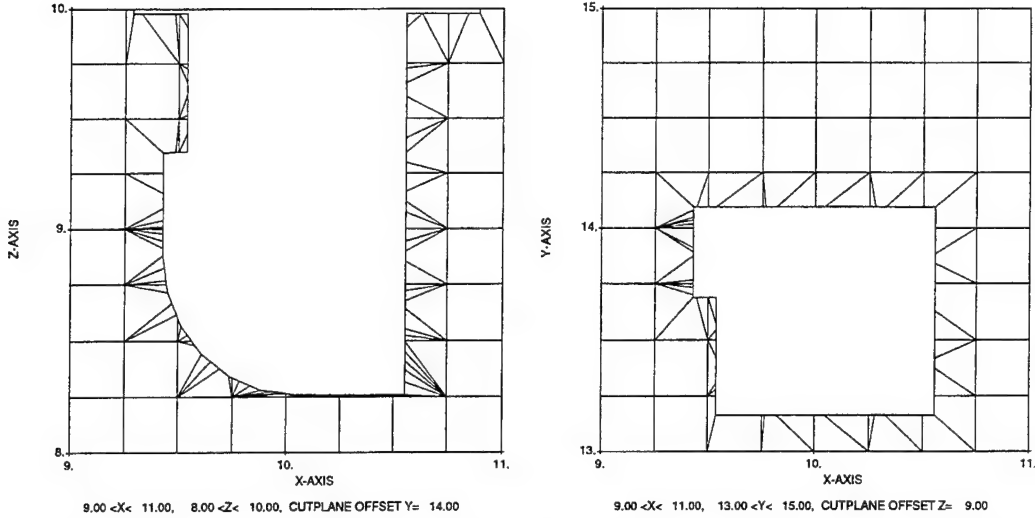


Figure 9. Figures used to determine aperture location in grid co-ordinates.

We surveyed all the macroparticles hitting the screen within 10° of the normal in the X-Z plane and within 10° of the normal to the X-Z plane.

Algebraically—Let (x,y,z) be the direction from the point of incidence on the screen to $(10.3, 13.95, 8.9)$. Let (u,v,w) be the direction of travel at the point of incidence. The criteria are then

$$\alpha \cos \left(\frac{ux + zw}{\sqrt{(x^2 + z^2)(u^2 + w^2)}} \right) \leq 10^\circ \quad (6)$$

$$\alpha \cos \left(\frac{u}{\sqrt{(u^2 + v^2)}} \right) \leq 10^\circ \quad (7)$$

The macroparticles were then binned by angle from vertical. The angle is

$$\alpha \cos \left(\frac{w}{\sqrt{(u^2 + v^2 + w^2)}} \right) \quad (8)$$

Figure 10 shows the incident flux as a function of shuttle potential and incident bin.

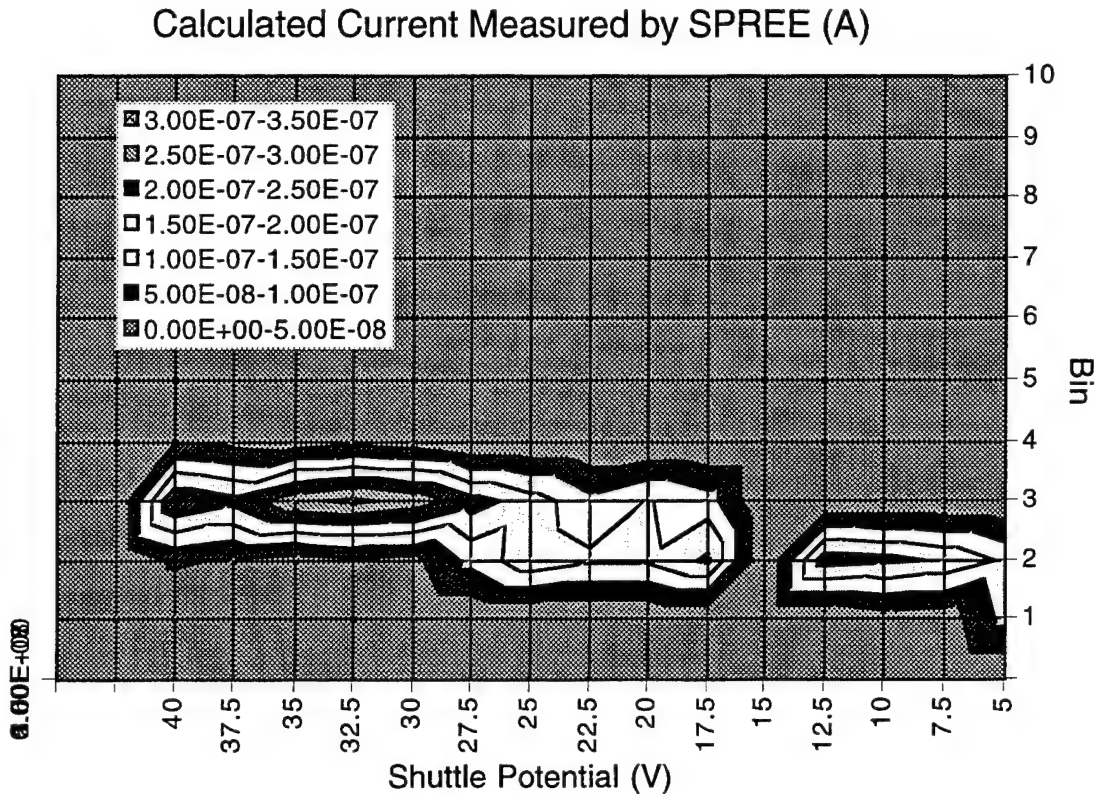


Figure 10. Computed ion flux as a function of shuttle potential and incident bin.

The similarity between Figures 4 and 10 indicates that the local potentials due to the shape of SPREE create the dependence of incident angle on shuttle potential.

3.2 SPREE Measurements During DEP1 Operations

During DEP1 operations, a sequence of resistors was inserted into the tether circuit and the FPEG electron gun was cycled. We only address charging data obtained when the gun was off. The largest resistance ($2.5 \text{ M}\Omega$) was orders of magnitude larger than the tether resistance (2200Ω). When switched into the tether circuit, the voltage measured at the orbiter was the $v \times B \cdot l$ generated by the tether moving through the earth's magnetic field, since the subsatellite floating potential was only a few kT. For smaller resistances, the maximum current that the induced EMF could drive through the tether resistance was often greater than the ion current that the orbiter could collect. When this occurred, the

orbiter charged to a negative potential . The steady state orbiter potential was such that the sheath drop at the orbiter reduced the voltage across the tether enough to reduce the tether current to the available orbiter ion current. The voltage drop in the tether is product of the tether current and resistance, both of which are known. The sheath drop, and therefore the orbiter potential, is just the difference between the available EMF and the voltage drop in the tether. The sheath drop at the subsatellite, as measured by RETE, was very small when FPEG was not operating.

In Figure 11, the orbiter potentials for 11 DEP1 cycles where charging occurred calculated from the tether current and voltage measurements are compared with the orbiter potential as reported by SPREE. The orbiter charged as much as 26 V negative, about 50 percent of the available motion induced $v \times B$. The largest negative potentials correspond to low ionosphere densities where the available ram ion current is smallest. When the available current is small the resistive voltage drop in the tether is small. The magnitude of the ram ion current is consistent with an effective ram facing exposed conducting area of about 23 m^2 . This number agrees with preflight calculations performed using a three dimensional spacecraft charging model of the orbiter. Those calculations show that most of the collection is by main engine bells. Thus, the orbiter potentials as measured ion energies, SPREE, and by insertion of a high impedance in the tether, SETS, both agree with the basic theory that the limited ion sheath current drives the orbiter potential. The higher the available ion current, the less the charging.

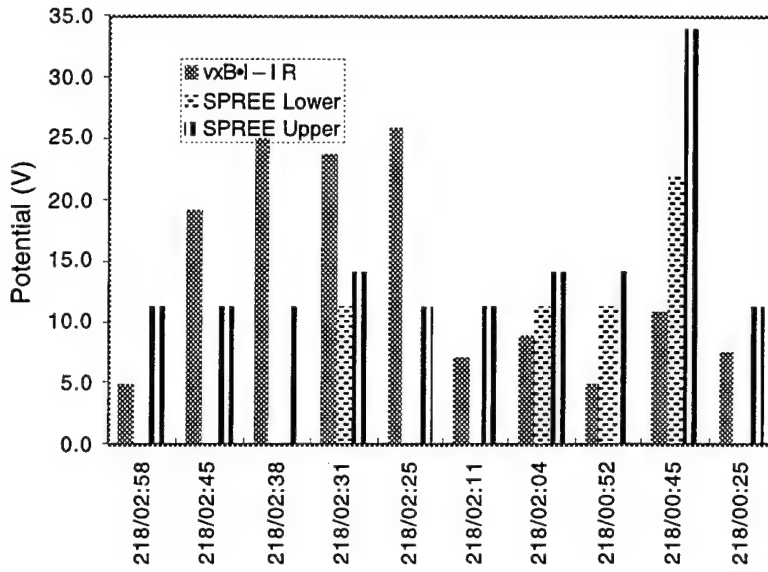


Figure 11.

The SPREE results, with their associated uncertainty due to the detector energy bin widths, agree quite well with the tether results. The SPREE potential is shown as the top and bottom of the detector energy channel which contains the most counts. The SPREE algorithm reports the middle of the energy channel. Note that the SPREE results were obtained in real time. The SETS potentials are based on tether currents and voltages measured at two different times, and depend on the particular operational sequences and accurate subsatellite sheath potentials. These measurements will not be available at high potentials (long tether lengths) and magnetic limiting of electron collection (low plasma densities), or when the DCORE electron gun is operating. Under those conditions, only the SPREE potentials will be available.

3.3 Shunter Orbit

A synoptic comparison of SPREE measurements over an entire orbit can be made with potentials calculated using the measured tether current and a model of the $v \times B$ induced EMF. During an entire orbit from 218/10:45 to 218/12:15, the tether was connected through a low resistance shunt to the orbiter chassis. The orbiter potentials as measured by SPREE are plotted in Figure 12. The plot shows clearly that the SPREE resolution is limited by the instrument energy bin widths.

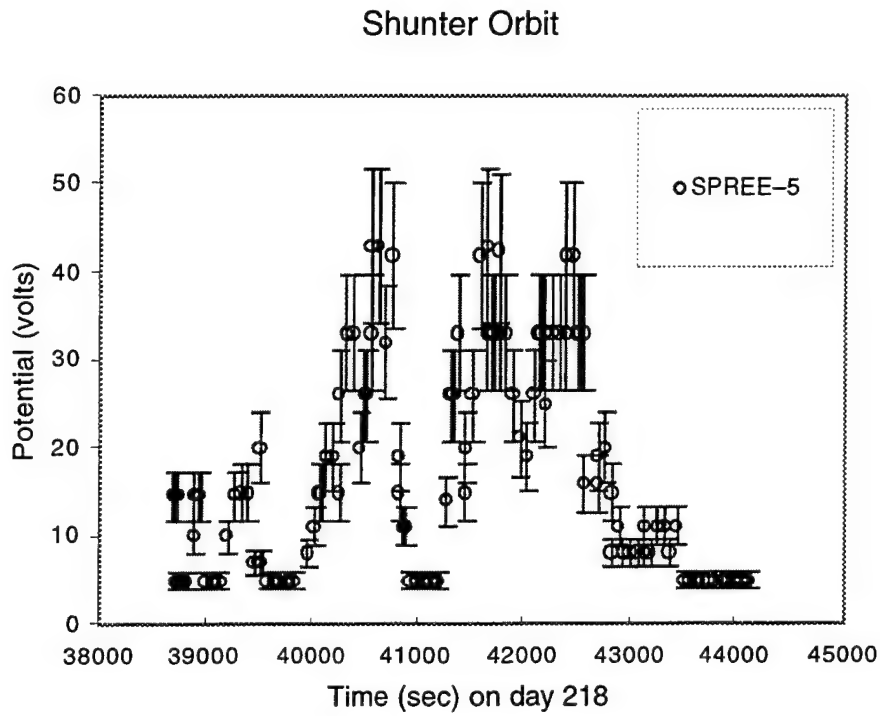


Figure 12. Orbiter potentials as measured by SPREE.

The tether current, as measured by SETS, is shown in Figure 13. Note that the orbiter charges when the tether current is very small, which occurs when the ambient ionosphere density is low. The reason that the charging levels increase when the tether voltage decreases can be seen in Figure 14. Plotted in this figure are the model available EMF, the tether voltage drop (the product of the measured tether current from SETS and the tether resistance), and the difference, which is the potential drop across the sheath which forms between the charged orbiter and the ionosphere. The tether resistance value used here is 2200Ω . The charging occurs when the resistive voltage drop (product of tether current and resistance) is small, leaving most of the motion induced EMF to be dropped across the electron collecting sheath at the subsatellite, and the ion collecting sheath at the orbiter. For these low potentials, the earth's magnetic field does not limit the electron collection. Most of the potential drop occurs across the orbiter ion collecting sheath.

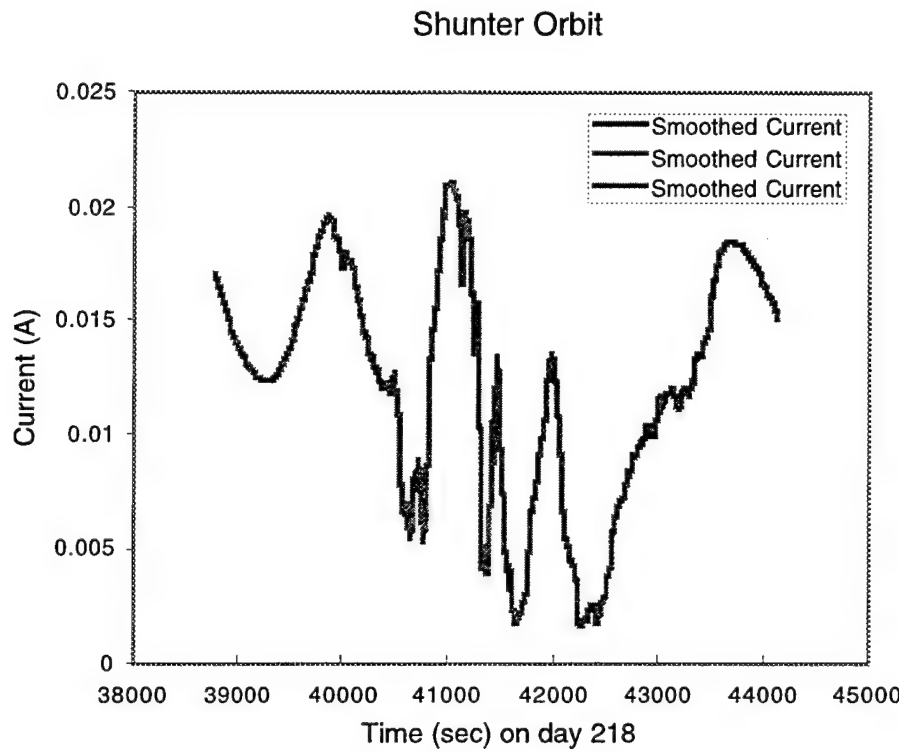


Figure 13. Tether current as measured by SETS.

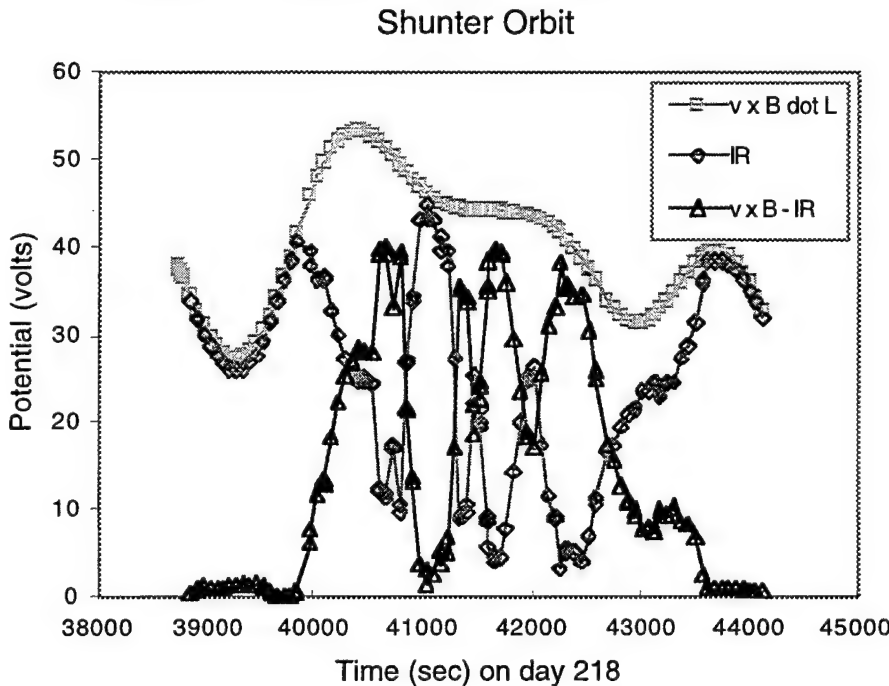


Figure 14. Model available EMF values, tether voltage drop (the product of the measured tether current from SETS and the tether resistance), and the difference, which is the potential drop across the sheath which forms between the charged orbiter and the ionosphere.

This calculation of the orbiter potential is compared with the SPREE result in Figure 15. Over the large range of plasma parameters encountered during the orbit, the two methods of calculating the orbiter potential are in agreement. Once again, however, the calculation using the tether current will not be available during gun operations and for very low potentials. With the DCORE electron gun operational or at high (kilovolt) potentials, only the SPREE results will be available.

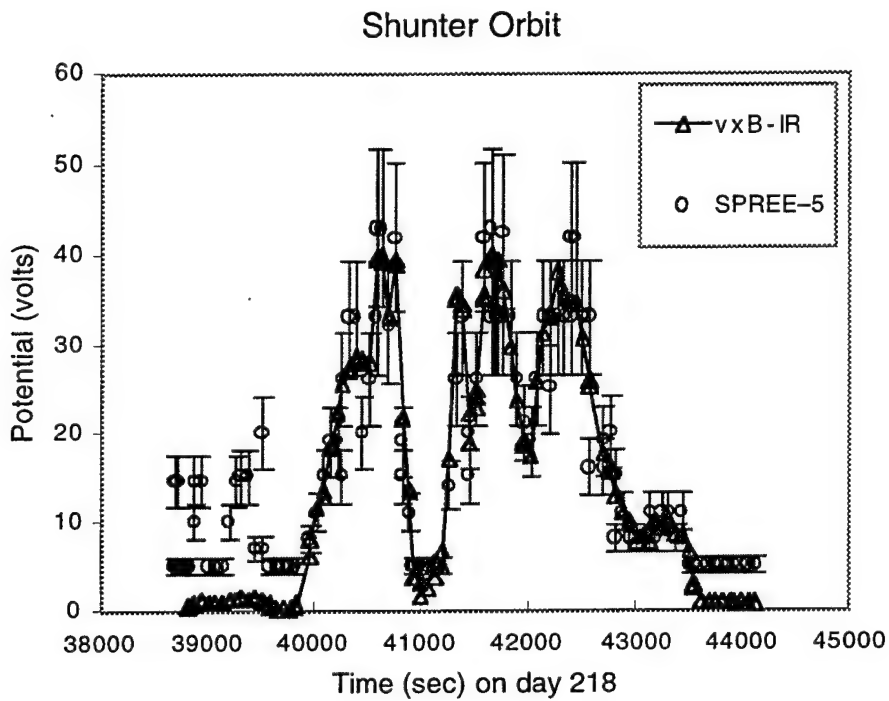


Figure 15. Orbiter potential as measured by SPREE and as computed from the available EMF and the tether current.

3.4 Conclusions

SPREE measured ram ions accelerated in a local sheath. There was no evidence of locally generated ions. A direct comparison with other measurements confirms SPREE potential measurements. SPREE will provide real time potentials at high potentials when the subsatellite is no longer at ionosphere potential.

4. EPSAT WAKE STUDIES SCREEN

The EPSAT Wake Studies screen uses the neutral approximation to compute the densities and current densities (as it would be measured by an RPA) of the neutral and plasma species in front of or behind a disk. The input parameters are the disk parameters, the spacecraft velocity, the ambient neutral and plasma environment, the point of interest, the look direction, and the incident energy.

The disk is described by its normal, its radius, and the location of its center. The normal of either the ram facing side or the wake facing side can be given.

By default the spacecraft velocity is given by the EPSAT orbit generator.

The ambient neutral and plasma environments are shown on the Neutral Density at a Point and Plasma Density at a Point screens. The density of each neutral and ion species and the neutral and ion temperatures are used.

The point of interest can be specified either by specifying an origin and a distance from that origin in spherical coordinates or directly in Cartesian coordinates.

The look direction can be specified either in terms of the spherical coordinate angles or in Cartesian coordinates. This parameter is only used for the current density computation.

The incident energy is given in electron volts. This parameter is only used for the current density computation. If the energy is negative, the current density is zero.

4.1 Densities

On the ram facing side of the disk, the densities are the ambient densities. The point of interest is on the ram facing side if the dot product of the normal of the wake facing side of the disk with the vector from the center of the disk to the point of interest is negative.

On the wake facing side of the disk, the density for each species is the integral

$$\rho(\mathbf{r}) = \rho_a (\pi T)^{-3/2} \int d\Omega dE \sqrt{E} g(\mathbf{r}, \theta, \phi) \exp\left(-\left(\frac{E + E_{\text{ram}} + 2\sqrt{EE_{\text{ram}}} \cos\theta}{T}\right)\right) \quad (9)$$

The ambient density of the species is ρ_a . The ion temperature is T . The vector \mathbf{r} is the vector from the center of the disk to the point of interest. The energy E is the incident particle energy. The energy E_{ram} is given by

$$E_{\text{ram}} = \frac{1}{2} m_s v_{\text{ram}}^2 \quad (10)$$

where m_s is the mass of the species and v_{ram} is the spacecraft velocity. The integral is done over the polar coordinates θ and ϕ , representing the negative of the incoming particle's velocity direction, where the origin for the integral is at the point of interest and θ is measured from the negative spacecraft velocity direction. The function g is zero if the direction given by θ and ϕ is blocked by the disk and unity otherwise.

The integral is solved differently for the case where the disk is normal to the spacecraft velocity and where it is not. A different technique is also used for the case in which the point of interest is directly behind the disk and where it is to the side.

4.2 Solution Technique for Normal Orientation and Point Directly Behind Disk

The outermost integral over the azimuthal angle, ϕ , is performed taking zero as the direction to the nearest disk edge point. To get a concentration of points near the nearest edge point, we define $\psi = \phi^{1/2}$. The minimum value of $\cos\theta$ can be shown to be

$$\begin{aligned} u_{\min}(\phi) &= -\left[1 + (x/z)^2\right]^{1/2} \\ x/r &= -\cos\phi + \left[\cos^2\phi + (R/r)^2 - 1\right]^{1/2} \end{aligned} \quad (11)$$

(The maximum value of $\cos\theta$ is 1, for particles overtaking the spacecraft from behind.) The energy variable is transformed by $t = e^{-E/E_0}$, where E_0 is an enerutational convenience. It is taken to be

$$E_0 = \left(\frac{m}{2e}\right) \frac{\left(V + 5\sqrt{\frac{2eT}{m}}\right)^2}{\ln(n_t)} \quad (12)$$

where n_t is the number of integration points used for the t-variable (i.e., energy). (Note: E_0 should be set to at least the ion temperature, T .)

After appropriate manipulation, the density at a point in the wake of the disk is given by

$$\frac{\rho}{\rho_a} = \pi^{-3/2} \frac{E_0}{\sqrt{T E_{ram}}} e^{-E_{ram}/T} \int_0^{\sqrt{\pi}} \psi d\psi \int_0^1 dt K(\psi, t) \quad (13)$$

$$K(\psi, t) = t^{\left(\frac{E_0}{T}-1\right)} \left\{ e^{-\gamma(t) u_{\min}(\psi)} - e^{-\gamma(t) u_{\max}(\psi)} \right\}$$

$$\gamma(t) = \sqrt{\frac{-4 E_0 E_{ram} \ln t}{T^2}}$$

Note that, to avoid overflows, all the exponents (including the one in the prefactor) should be grouped together, so that the only exponentiations are the two in the inner loop.

EPSAT performs the integrals numerically.

4.3 Solution Technique for Normal Orientation and Point Not Directly Behind Disk

The integral is over those trajectories blocked by the disk, and the result subtracted from unity. The outer integral is over the angle between the look direction and the vector toward the ram, which takes the range

$$\frac{1}{\sqrt{1+\left(\frac{R+r}{z}\right)^2}} < u = \cos\theta < \frac{1}{\sqrt{1+\left(\frac{r-R}{z}\right)^2}} \quad (14)$$

To concentrate points toward the ram direction, the integration variable is changed to $w = \sqrt{1-u}$. The integral over azimuthal angles contributes a factor

$$\Delta\phi(u) = 2 \arccos \left\{ \frac{\left[(r^2 - R^2 - z^2) u^2 + z^2 \right]}{\left[2 r z u (1-u^2)^{1/2} \right]} \right\} \quad (15)$$

The final result is

$$1 - \frac{\rho}{\rho_0} = \left[\frac{E_0}{\pi T} \right]^{3/2} e^{-\frac{E_{ram}}{T}} \int_{\sqrt{1-u_{max}}}^{\sqrt{1-u_{min}}} w dw \Delta\phi(1-w^2) \int_0^1 dt K(1-w^2, t) \quad (16)$$

$$K(u, t) = t^{\left(\frac{E_0}{T}-1\right)} e^{\gamma(t)u} (-lnt)^{1/2}$$

$$\gamma(t) = \sqrt{\frac{-4 E_0 E_{ram} lnt}{T^2}}$$

4.4 Solution Technique for Other Orientations

If the normal to the disk is not parallel to the velocity, the problem is solved similarly, although the geometry is more complex.

First, the disk and the field point are projected onto a plane normal to the velocity (Z), so that the disk edge is an ellipse with its major axis in the X direction.

$$x^2 + \alpha y^2 = R^2 \quad (17)$$

The point (x, y) on the ellipse nearest the field point projection (x_0, y_0) (for the first quadrant) satisfies

$$x(\alpha - 1) - \alpha x_0 + xy_0 \sqrt{\frac{\alpha}{R^2 - x^2}} = 0 \quad (18)$$

When (x_0, y_0) lies inside the ellipse, the outer angular integral is over the angle, ϕ , from the field point to the wake edge, given by

$$\phi = \arctan \left[\frac{y - y_0}{x - x_0} \right] \pm \psi^2 \quad (19)$$

where the integration variable, ψ , concentrates near the presumed integrand peak at (x, y) . There are two values of u_{\min} (the cosine of the angle between the direction from the field point to the disk edge and the negative velocity direction) for each ψ , obtained by calculating the disk edge point $(x_0 + d \cos\phi, y_0 + d \sin\phi, z_1)$. The values are determined by first solving the ellipse equation d , then the circle equation for z_1 . Then

$$u_{\min} = \frac{z_0 - z_1}{\sqrt{d^2 + (z_0 - z_1)^2}} \quad (20)$$

where the sign of z_1 is opposite the sign of $y_0 + d \sin\phi$. The energy integral then proceeds as for the velocity-aligned case, except that the normalization must take account of the asymmetry in the ϕ integral.

When (x_0, y_0) lies outside the ellipse, the integral is over the region from which ions are excluded and the normalized result subtracted from unity. The outer angular integral is over the variable u (the cosine of the angle between the ram direction and the direction from the field point to a point on the disk), which goes from the angle corresponding to the near point of the disk to the diametrically opposite point. For each u , there are two values of ϕ that satisfy both the disk edge equation and the defining equation for u :

$$\begin{aligned}
(x_0 + d \cos \phi)^2 + \alpha(y_0 + d \sin \phi)^2 &= R^2 \\
(x_0 + d \cos \phi)^2 + (y_0 + d \sin \phi)^2 + z^2 &= R^2 \\
z(y_0 + d \sin \phi) &\leq 0 \\
u &= \frac{z - z_0}{\sqrt{d^2 + (z - z_0)^2}}
\end{aligned} \tag{21}$$

The difference between the two ϕ values corresponds to the $\Delta\phi(u)$ that appears in the velocity-aligned case.

4.5 Current Densities

The differential ram ion current density to a detector in the presence of a disk is zero if the detector is looking at the disk. Otherwise it is given by the following formula.

$$j(E, \Omega) = \int_E^{32 \text{ eV}} \frac{e n}{\pi} \frac{E_i}{\theta^2} \sqrt{\frac{e \theta}{2 \pi m}} \exp\left(-\frac{m}{2 e \theta} (v_i + v_s)^2\right) dE_i \tag{22}$$

The quantity v_i is the velocity of the incident ions (ions at energy E_i incident in the look direction). The quantity v_s is the velocity of the detector and the disk (negative the ram velocity).